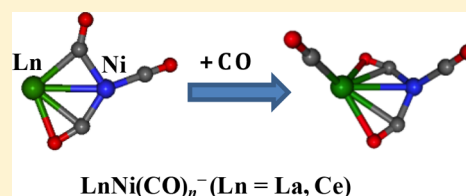


Ligand-Enhanced CO Activation by the Early Lanthanide–Nickel Heterodimers: Photoelectron Velocity-Map Imaging Spectroscopy of $\text{LnNi}(\text{CO})_n^-$ ($\text{Ln} = \text{La}, \text{Ce}$)

Gang Li,^{†,§} Jumei Zhang,^{†,‡,§} Hua Xie,[†] Xiangtao Kong,[†] and Ling Jiang^{*,†,§}[†]State Key Laboratory of Molecular Reaction Dynamics, Dalian Institute of Chemical Physics, Chinese Academy of Sciences, 457 Zhongshan Road, Dalian 116023, China[‡]University of Chinese Academy of Sciences, 19A Yuquan Road, Beijing 100049, China

Supporting Information

ABSTRACT: Heterobimetallic lanthanum–nickel and cerium–nickel carbonyls, $\text{LnNi}(\text{CO})_n^-$ ($\text{Ln} = \text{La}, \text{Ce}; n = 2-5$), were generated using a pulsed laser vaporization/supersonic expansion ion source. These compounds were characterized by photoelectron velocity-map imaging spectroscopy and quantum chemical calculations. The binding motif in the most stable isomers of the $n = 2$ and 3 clusters consists of one side-on-bonded carbonyl. A new building block of two side-on-bonded carbonyls is favored at $n = 4$, which is retained at $n = 5$, evidencing the increase of the number of extremely activated CO molecule in the larger clusters. The experimental and theoretical results demonstrate the ligand-enhanced CO activation by the early lanthanide–nickel heterodimers, which would have important implications for the design of alloy catalysts for activation of a molecular ligand.



1. INTRODUCTION

Metal clusters may represent the low-coordinate sites on the surface and are often regarded as models for the surface of bulk materials.¹⁻⁵ Under well-defined conditions, the reaction between those clusters and the reactants could provide the structural and energetic information for molecular-level understanding of a catalytic process, which is not readily accessible from conventional bulk measurements.³⁻¹⁰ The reactions of CO with metal clusters are directly relevant to many catalytic processes, such as Fischer–Tropsch chemistry, acetic acid synthesis, alcohol synthesis, and hydroformylation.^{3,8,11-13} Homobimetallic metal carbonyls have been explored experimentally and theoretically, which afford the smallest model for the reactions of CO with metal clusters.^{12,14-29}

Recently, the study on the reaction of CO with heteronuclear metal clusters has aroused increasing attention, which helps uncover the diverse structural features, the nature of chemical bonding, and the synergy effects of different transition metals on the catalytic performance.²⁹⁻³⁸ In the heterobimetallic metal–iron carbonyls, $\text{PbFe}(\text{CO})_4^-$ and $\text{CuFe}(\text{CO})_4^-$, the CO ligands are terminally bonded to the iron atom.^{32,34} The $\text{MFe}(\text{CO})_8^+$ ($\text{M} = \text{Co}, \text{Ni}, \text{Cu}$) cations are comprised of eclipsed $(\text{CO})_5\text{Fe}-\text{M}(\text{CO})_3^+$ motif and $\text{MCu}(\text{CO})_7^+$ ($\text{M} = \text{Co}, \text{Ni}$) consist of staggered $(\text{CO})_4\text{M}-\text{Cu}(\text{CO})_3^+$ motif, where the CO molecules are terminally coordinated to the metal atoms.³⁹ The $\text{ZnFe}(\text{CO})_5^+$ carbonyl consists of a $\text{Zn}-\text{Fe}(\text{CO})_5$ structure with a $\text{Zn}-\text{Fe}$ half bond and $\text{ZnCo}(\text{CO})_7^+$ has a staggered $\text{Zn}(\text{CO})_3-\text{Co}(\text{CO})_4$ structure involving a $\text{Zn}-\text{Co}$ σ single bond.³⁶ Interestingly, $\text{UFe}(\text{CO})_3^-$ and $\text{OUFe}(\text{CO})_3^-$ were determined to have triple bonds between U 6d/5f and Fe 3d

orbitals, which feature one covalent σ bond and two Fe-to-U dative π bonds.³⁸

In contrast, the $\text{Ni}(\text{CO})_3$ building block is involved in the $\text{MNi}(\text{CO})_3^-$ ($\text{M} = \text{Mg}, \text{Ca}, \text{Al}$) complexes.³³ The carbonyl groups were found to be terminally coordinated to the nickel atom in the $\text{MNi}(\text{CO})_3^-$ ($\text{M} = \text{Cu}, \text{Ag}$) clusters.^{31,35} Interestingly, the $\text{MNi}(\text{CO})_3^-$ ($\text{M} = \text{Ti}, \text{Zr}, \text{Hf}$) carbonyls are capable of accommodating three different types of CO coordination configuration (i.e., side-on-bonded, bridging, and terminal modes).³⁷

Lanthanide compounds are widely applied in various fields such as catalysis, biology, medicine, and optics.⁴⁰⁻⁴² The $\text{Ni}(\text{CO})_4$ carbonyl was the first metal carbonyl prepared in 1890,⁴³ and nickel group carbonyls have been extensively explored by various types of experimental and theoretical methods.¹¹ The investigation of the reaction of CO with the lanthanide–nickel heterodimers would be helpful for a molecular understanding of the interaction of CO with the alloy surfaces/interfaces and for the development of new catalysts.^{3,4,8,30} Herein, we use photoelectron velocity-map imaging spectroscopy of mass-selected $\text{LnNi}(\text{CO})_n^-$ ($\text{Ln} = \text{La}, \text{Ce}$) complexes to study CO activation by the lanthanum–nickel and cerium–nickel heterodimers.

Received: March 7, 2018

Revised: April 2, 2018

Published: April 2, 2018

2. EXPERIMENTAL AND COMPUTATIONAL METHODS

The experiments were carried out using photoelectron velocity-map imaging spectroscopy. The description of this apparatus has been detailed previously.⁴⁴ The $\text{LnNi}(\text{CO})_n^-$ ($\text{Ln} = \text{La}, \text{Ce}$) species were produced using laser-vaporization cluster source, and these cluster anions were generated in a supersonic expansion of 5% CO seeded in helium (purity: 99.9999%). A 532 nm laser beam from a Nd:YAG laser (Continuum, Minilite II, 10 Hz repetition rate and 6 ns pulse width) was used to ablate the metal target ($\text{Ln}:\text{Ni} = 1:1$ molar ratio). For the vaporization laser, the pulse energy was ~ 10 mJ and the diameter of laser beam was focused to be ~ 0.2 mm. The typical stagnation pressure of the carrier gas was ~ 5 atm. The species were skimmed into the source chamber. These anionic clusters were mass-selected by a McLaren Wiley time-of-flight (TOF) mass spectrometer. The species of interest was mass-selected into the photodetachment region and crossed with a laser beam. Photon energies of 532 nm (2.331 eV) and 355 nm (3.496 eV) were used to photodetach these anionic clusters. The photoelectrons were detected using a microchannel plate (MCP)/phosphor screen combination, and the resulting photoelectron images were collected using a charge-coupled device (CCD) camera. The basis set expansion (BASEX) inverse Abel transform method was used to reconstruct the original 3D distribution.⁴⁵ The photoelectron spectrum was obtained by integrating one central slice of the 3D distribution. The photoelectron kinetic energy spectra were calibrated using the known spectrum of Au^- . The energy resolution was better than 5%, corresponding to 50 meV at electron kinetic energy (eKE) of 1 eV.

The TURBOMOLE V6.4 program was used for all calculations.⁴⁶ The B3LYP hybrid functional was employed. The def-TZVPP basis set was used for the La and Ce atoms and the Aug-cc-pVTZ basis set was used for the C and O atoms. Possible spin configurations were considered. The theoretical vertical detachment energy (VDE) was calculated as the difference in the energy between the neutral and anionic species at the optimized anion geometry, and the theoretical adiabatic detachment energy (ADE) was computed as the difference in the energy between the neutral and anionic species both at their optimized geometries. The theoretical ADEs and relative energies included the zero-point-energy corrections. Test calculations were also performed for other available density functionals (i.e., BP86, PBE, PBE0, B3LYP, TPSS, TPSSH), which yielded essentially the similar structures. The scalar relativistic calculations were carried out by Douglas-Kroll-Hess second order approximation in Gaussian 09.⁴⁷ Singlet point energies were performed on the quasi-relativistic pseudopotentials optimized structures at the B3LYP level of theory with all electronic basis set Aug-cc-pVTZ-DK for the C and O atoms and x2c-TZVPPall for the metal atoms. The stick spectra of theoretical vertical detachment energies were convoluted using a Gaussian line shape function with a width of 0.1 eV.

3. EXPERIMENTAL RESULTS

The mass spectra obtained at the experimental conditions that favor the formation of anions with relatively high thermodynamic stability are given in Figures S1 and S2 in the Supporting Information, respectively. Besides the $\text{LnNi}(\text{CO})_n^-$ ($\text{Ln} = \text{Ce}, \text{La}$) target products, the $\text{Ni}(\text{CO})_3^-$ and $\text{LnNiO}(\text{CO})_n^-$ complexes were also observed. The homoleptic $\text{Ln}(\text{CO})_n^-$ carbonyl anions were barely observed.

The 532 nm photoelectron imaging and photoelectron spectra of $\text{LnNi}(\text{CO})_n^-$ ($\text{Ln} = \text{Ce}, \text{La}; n = 2-5$) are shown in Figures 1 and 2, respectively, and those of the 355 nm

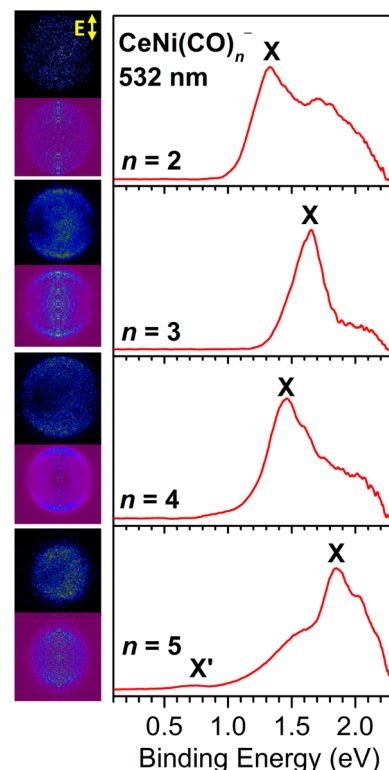


Figure 1. Photoelectron images of $\text{CeNi}(\text{CO})_n^-$ ($n = 2-5$) at 532 nm (2.331 eV). The raw image (upper) and the reconstructed image (bottom) after inverse Abel transformation are shown on the left side. The double arrow indicates the direction of the laser polarization. Photoelectron spectra are shown on the right side.

photoelectron imaging and photoelectron spectra are depicted in Figures S3 and S4. The 532 nm spectra afford better resolution of the X band. In the 532 nm spectrum of $\text{CeNi}(\text{CO})_4^-$ (Figure 1), the low electron-binding-energy edge of the main peak (1.25 eV) is much broader than for the smaller clusters, suggesting that there is an unresolved feature underneath. In the 532 nm spectrum of $\text{CeNi}(\text{CO})_5^-$, a very weak band (labeled X') appears around 0.70 eV, which might be due to an excited state of the anion. Similar features have also observed in the photoelectron spectra of the ScO^- and YO^- anions.⁴⁸ A partially resolved shoulder at 1.65 eV appears in the 532 nm spectrum of $\text{CeNi}(\text{CO})_5^-$, which could be due to other low-lying isomers. Analogous features also appear in the 532 nm spectra of $\text{LaNi}(\text{CO})_4^-$ and $\text{LaNi}(\text{CO})_5^-$ (Figure 2). However, the X bands were observed in the 355 nm spectra (Figures S3 and S4), which confirm the assignment of the ground state (X). For each cluster, the experimental VDE was determined from the maximum of the X band in the 532 nm photoelectron spectrum and the experimental ADE was evaluated by drawing a straight line at the rising edge of the X band. The experimental VDEs and ADEs of $\text{LnNi}(\text{CO})_n^-$ ($\text{Ln} = \text{Ce}, \text{La}; n = 2-5$) are summarized in Tables 1 and 2, respectively.

The experimental VDEs of $\text{CeNi}(\text{CO})_n^-$ ($n = 2-5$) complexes were determined to be 1.33 ± 0.11 , 1.63 ± 0.09 , 1.46 ± 0.10 , and 1.85 ± 0.08 eV (Table 1), respectively. The

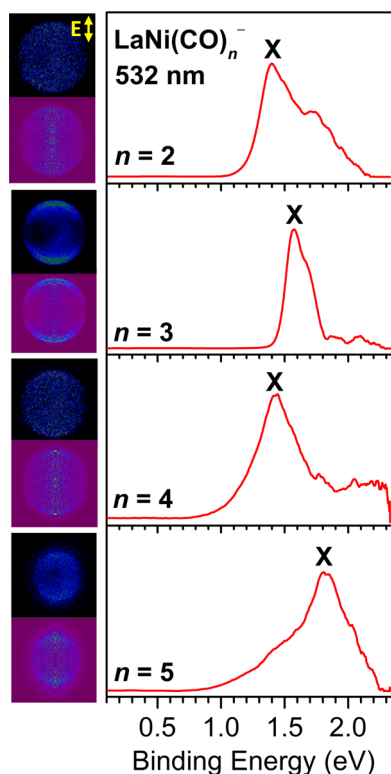


Figure 2. Photoelectron images of $\text{LaNi}(\text{CO})_n^-$ ($n = 2-5$) at 532 nm (2.331 eV). The raw image (upper) and the reconstructed image (bottom) after inverse Abel transformation are shown on the left side. The double arrow indicates the direction of the laser polarization. Photoelectron spectra are shown on the right side.

Table 1. Comparison of Experimental VDE and ADE Values to B3LYP Calculated Ones and Relative Energies (ΔE) of the Isomers for $\text{CeNi}(\text{CO})_n^-$ ($n = 2-5$)

cluster	isomer	ΔE (eV)	VDE (eV)		ADE (eV)	
			calcd	expt ^a	calcd	expt ^a
$\text{CeNi}(\text{CO})_2^-$	2A	0.00	1.29	1.33(11)	1.23	1.18(12)
	2B	0.07	1.10		1.00	
	2C	0.39	1.10		1.26	
	2D	1.01	1.11		1.05	
$\text{CeNi}(\text{CO})_3^-$	3A	0.00	1.46	1.63(9)	1.40	1.50(10)
	3B	0.17	1.00		0.84	
	3C	0.53	1.02		1.07	
	3D	0.85	1.08		1.31	
$\text{CeNi}(\text{CO})_4^-$	4A	0.00	1.54	1.46(10)	1.38	1.31(11)
	4B	0.20	1.43	1.25(10)	1.41	1.21(11)
	4C	0.39	1.39		1.31	
	4D	0.52	2.01		1.35	
$\text{CeNi}(\text{CO})_5^-$	5A	0.00	1.95	1.85(8)	1.67	1.72(9)
	5B	0.10	1.82	1.65(8)	1.70	1.56(9)
	5C	0.32	1.86		1.59	
	5D	0.73	1.79		1.53	

^aNumbers in parentheses represent the uncertainty in the last digits.

experimental ADEs of $\text{CeNi}(\text{CO})_n^-$ ($n = 2-5$) were evaluated to be 1.18 ± 0.12 , 1.50 ± 0.10 , 1.31 ± 0.11 , and 1.72 ± 0.09 eV (Table 1), respectively.

The 532 nm photoelectron images and spectra of $\text{LaNi}(\text{CO})_n^-$ ($n = 2-5$) are close to those of $\text{CeNi}(\text{CO})_n^-$ (Figures 1 and 2). The experimental VDEs of $\text{LaNi}(\text{CO})_n^-$ ($n = 2-5$)

were measured to be 1.40 ± 0.10 , 1.58 ± 0.09 , 1.44 ± 0.10 , and 1.81 ± 0.08 eV (Table 2), respectively. The experimental ADEs of $\text{LaNi}(\text{CO})_n^-$ ($n = 2-5$) were estimated to be 1.20 ± 0.11 , 1.40 ± 0.10 , 1.28 ± 0.11 , and 1.63 ± 0.09 eV (Table 2), respectively.

4. COMPARISON BETWEEN EXPERIMENTAL AND THEORETICAL RESULTS

Figures 3 and S5 show the optimized structures of $\text{LnNi}(\text{CO})_n^-$ ($\text{Ln} = \text{Ce}, \text{La}; n = 2-5$), respectively. The comparison of experimental VDEs and ADEs to the B3LYP calculated values of the four lowest-energy isomers for $\text{LnNi}(\text{CO})_n^-$ ($\text{Ln} = \text{Ce}, \text{La}; n = 2-5$) is given in Tables 1 and 2, respectively. Test calculation results of $\text{CeNi}(\text{CO})_n^-$ ($n = 2-5$) at the TPSSH/def-TZVPP/Aug-cc-pVTZ level of theory are shown in Table S1. It can be seen that the B3LYP calculated VDE values of the $\text{LnNi}(\text{CO})_n^-$ ($\text{Ln} = \text{La}, \text{Ce}; n = 2-5$) complexes agree best with experiment. Relativistic calculations have been tested for $\text{CeNi}(\text{CO})_3^-$. The scalar relativistic calculated VDE values of the 3A, 3B, 3C, and 3D isomers are 1.46, 1.03, 1.05, and 1.11 eV, respectively, which are consistent with the B3LYP/def-TZVPP/Aug-cc-pVTZ calculated values of 1.46, 1.00, 1.02, and 1.08 eV. Accordingly, only the B3LYP/def-TZVPP/Aug-cc-pVTZ calculated results are used for the present discussions.

$\text{CeNi}(\text{CO})_2^-$. For $\text{CeNi}(\text{CO})_2^-$, the lowest-energy isomer (labeled as 2A) has a C_s structure with a $^4A'$ ground state (Figure 3) and contains one side-on-bonded carbonyl and one terminal carbonyl bonded to the Ni atom. The 2B isomer (+0.07 eV) is comprised of two side-on bonded carbonyls. The 2C isomer has one side-on-bonded carbonyl and one bridging carbonyl, which lies higher in energy above 2A by 0.39 eV. The 2D isomer consists of one bridging carbonyl and one terminal carbonyl, which lies higher in energy above 2A by 1.01 eV. As listed in Table 1, the calculated VDE and ADE values for the most stable structure of 2A (1.29 and 1.23 eV) agree well with the experiment values (1.33 ± 0.11 and 1.18 ± 0.12 eV), respectively. The calculated VDE and ADE values of 2B (1.10 and 1.00 eV) are also close to the experimental values. As shown in Figure 4, the simulated spectra of 2A and 2B are very similar and the main features were seen experimentally. The band positions and overall pattern of simulated spectrum of 2A is in slightly better agreement with experiment but the presence of 2B cannot be ruled out. A mixture of 2A and 2B (trace labeled Mix (2A + 2B)) improves the agreement between theory and experiment. Considering that the isomerization barrier from 2B to 2A is predicted to be small as 0.18 eV, the coexistence of the 2A and 2B isomers is likely here. The simulated spectra of isomers 2C and 2D fit worse with the experimental spectra with respect to 2A and 2B (Figure 4).

$\text{CeNi}(\text{CO})_3^-$. The most stable structure of $\text{CeNi}(\text{CO})_3^-$, labeled 3A, involves terminal, bridging, and side-on-bonded modes, in which the terminal CO is coordinated to the Ni atom (Figure 3). The structure of 3B (+0.17 eV) is comprised of one terminal and two side-on bonded carbonyls. The structure of 3C consists of three side-on bonded carbonyls, which lies 0.53 eV above 3A. The 3D isomer (+0.85 eV) has three bridging carbonyls. It can be seen from Table 1 that the calculated VDE and ADE of 3A (1.46 and 1.40 eV) are consistent with experiment (1.63 ± 0.09 and 1.50 ± 0.10 eV), respectively. The calculated VDEs of 3B (1.00 eV), 3C (1.02 eV), and 3D (1.08 eV) are much lower than the experimental value (1.63 ± 0.09 eV). The calculated photoelectron spectrum of 3A agrees best with experiment (Figure 5). The calculated photoelectron

Table 2. Comparison of experimental VDE and ADE values to B3LYP calculated ones and relative energies (ΔE) of the isomers for $\text{LaNi}(\text{CO})_n^-$ ($n = 2-5$)

cluster	isomer	ΔE (eV)	VDE (eV)		ADE (eV)	
			calcd	expt ^a	calcd	expt ^a
$\text{LaNi}(\text{CO})_2^-$	2-I	0.00	1.26	1.40(10)	1.21	1.20(11)
	2-II	-0.03	1.07		0.99	
	2-III	0.28	1.13		1.09	
	2-IV	1.09	1.12		1.09	
$\text{LaNi}(\text{CO})_3^-$	3-I	0.00	1.44	1.58(9)	1.40	1.40(10)
	3-II	0.08	0.94		0.89	
	3-II	0.53	1.03		1.45	
	3-III	0.94	1.08		1.00	
$\text{LaNi}(\text{CO})_4^-$	4-I	0.00	1.57	1.44(10)	1.43	1.28(11)
	4-II	0.12	1.52	1.20(10)	1.38	1.18(11)
	4-III	0.32	1.65		1.57	
	4-IV	0.57	1.39		1.31	
$\text{LaNi}(\text{CO})_5^-$	5-I	0.00	1.84	1.81(8)	1.58	1.63(9)
	5-II	0.20	1.71	1.53(8)	1.47	1.40(9)
	5-III	0.26	1.85		1.60	
	5-IV	0.76	1.68		1.58	

^aNumbers in parentheses represent the uncertainty in the last digits.

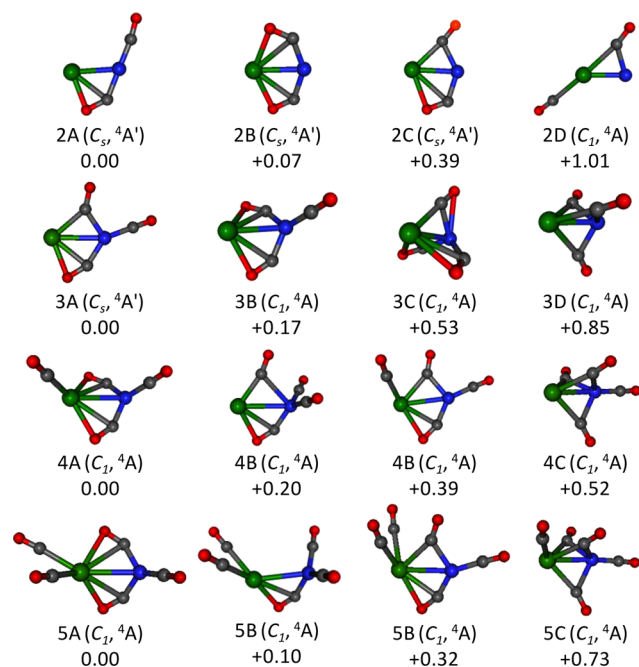


Figure 3. Optimized structures of the $\text{CeNi}(\text{CO})_n^-$ ($n = 2-5$) anions (Ce, green; Ni, blue; C, black; O, red). Relative energies are given in eV.

spectra of **3B**, **3C**, and **3D** are different from experiment, and these three isomers can be ruled out from the assignment.

CeNi(CO)₄⁻. The lowest-energy isomer of $\text{CeNi}(\text{CO})_4^-$ (**4A**) has two side-on-bonded carbonyls and two terminal carbonyls, in which one terminal carbonyl is coordinated to the Ce atom and another terminal carbonyl is bound to the Ni atom (Figure 3). Isomer **4B** (+0.20 eV) consists of two terminally coordinated COs, one bridging CO, and one side-on-bonded CO. Isomer **4C** is comprised of one bridging, one side-on-bonded, and two terminal carbonyls coordinated to the Ce and Ni atoms, respectively, which lies 0.39 eV above **4A**. The **4D** isomer (+0.52 eV) has three bridging carbonyls and one carbonyl terminally coordinated to the Ni atom. The

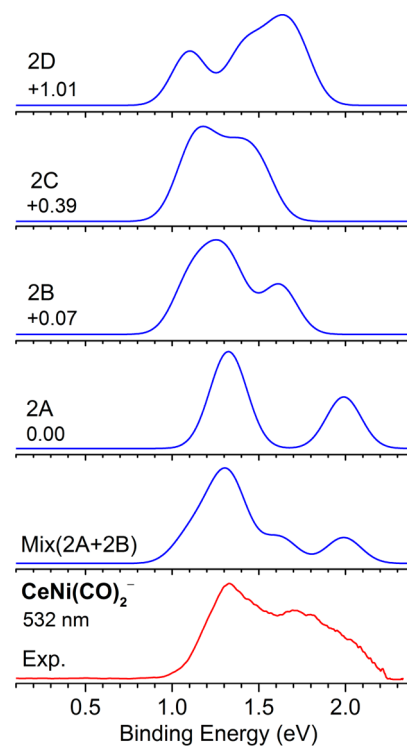


Figure 4. Comparison of experimental 532 nm photoelectron spectrum (bottom row) of $\text{CeNi}(\text{CO})_2^-$ to the simulated spectra of the isomers **2A–2D** (upper rows). Relative energies are given in eV. The trace labeled **Mix (2A + 2B)** denotes a 1:1 mixture of **2A** and **2B**.

calculated VDE and ADE of **4A** is 1.54 and 1.38 eV (Table 1), respectively, consistent with experiment (1.46 ± 0.10 and 1.31 ± 0.11 eV). The calculated VDE of **4B** (1.43 eV) (Table 1) is consistent with the broad feature at 1.25 ± 0.10 eV. As shown in Figure 6, the simulated spectra of **4A** and **4B** are very similar and better agreement is obtained by the **4A** and **4B** mixture. The intensity of the peak at 2.10 eV in the simulated spectra of **4A** and **4B** is reduced in the experiment, which could be due to the limit of photodetachment laser of 532 nm (2.331 eV). The

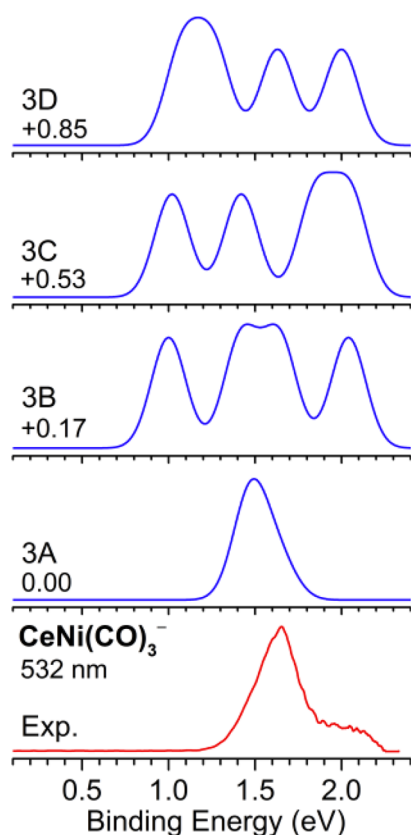


Figure 5. Comparison of experimental 532 nm photoelectron spectrum (bottom row) of $\text{CeNi}(\text{CO})_3^-$ to the simulated spectra of the isomers 3A–3D (upper rows). Relative energies are given in eV.

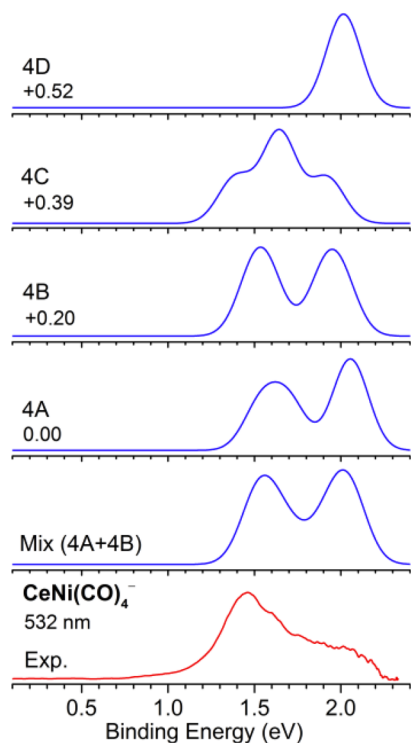


Figure 6. Comparison of experimental 532 nm photoelectron spectrum (bottom row) of $\text{CeNi}(\text{CO})_4^-$ to the simulated spectra of the isomers 4A–4D (upper rows). Relative energies are given in eV. The trace labeled Mix (4A + 4B) denotes a 1:1 mixture of 4A and 4B.

4C and 4D isomers could be ruled out by the mismatch of the simulated spectra with experiment.

$\text{CeNi}(\text{CO})_5^-$. In the lowest-energy isomer for $\text{CeNi}(\text{CO})_5^-$, 5A, two CO molecules are in the side-on-bonded configuration, two CO molecules are terminally coordinated to the Ce atom, and one CO molecule is terminally coordinated to the Ni atom (Figure 3). Isomer 5B (+0.10 eV) consists of one side-on-bonded COs, two terminal COs coordinated to the Ce atom, and two terminal COs coordinated to the Ni atom. Isomer 5C lies 0.32 eV above 5A and is comprised of two terminal COs coordinated to the Ce atom, and one terminal CO coordinated to the Ni atom, one bridging CO, and one side-on-bonded CO. Isomer 5D (+0.73 eV) contains three bridging COs and two terminal COs. The calculated VDE and ADE of 5A (1.95 and 1.67 eV) agree with experiment (1.85 ± 0.08 and 1.72 ± 0.09 eV) of the main band (Table 1), respectively. The calculated VDE of 5B (1.82 eV) (Table 1) is consistent with the shoulder feature at 1.65 ± 0.08 eV. As shown in Figure 7, the simulated spectra of the 5A and 5B mixture reproduce the experimental spectrum.

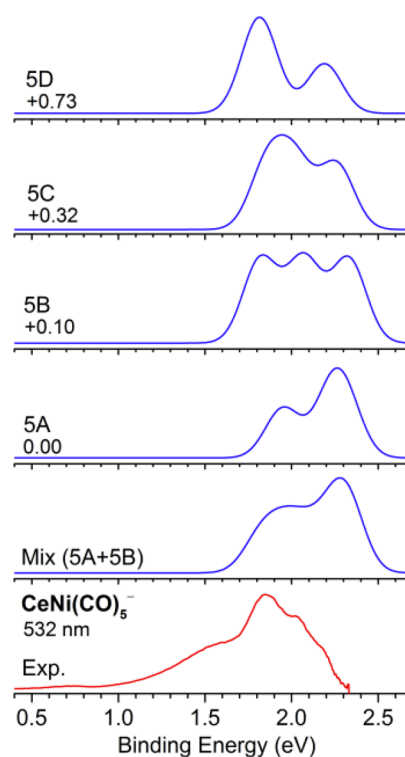


Figure 7. Comparison of experimental 532 nm photoelectron spectrum (bottom row) of $\text{CeNi}(\text{CO})_5^-$ to the simulated spectra of the isomers 5A–5D (upper rows). Relative energies are given in eV. The trace labeled Mix (5A + 5B) denotes a 1:1 mixture of 5A and 5B.

It can be seen from Figures 3 and S5 that the configurations for $\text{LaNi}(\text{CO})_n^-$ ($n = 2-5$) are similar to those of $\text{CeNi}(\text{CO})_n^-$. The agreement between the experimental and calculated VDEs and ADEs of $\text{LaNi}(\text{CO})_n^-$ is obtained (Table 2).

5. DISCUSSION

Overall agreement between the experimental and theoretical results allows for exploring the structural evolution of $\text{LnNi}(\text{CO})_n^-$ ($\text{Ln} = \text{Ce}, \text{La}; n = 2-5$). For $\text{CeNi}(\text{CO})_n^-$, the experimental VDE value of $n = 4$ is smaller than that of $n = 3$,

implying that the CO coordination mode of $\text{CeNi}(\text{CO})_4^-$ is different from $\text{CeNi}(\text{CO})_3^-$. It can be seen from the above analysis that the most stable structures of $\text{CeNi}(\text{CO})_n^-$ ($n = 2$ and 3) contain a motif of one side-on-bonded carbonyl. The **4A** isomer for $\text{CeNi}(\text{CO})_4^-$ includes two side-on-bonded carbonyls. The preferred structure of $\text{CeNi}(\text{CO})_5^-$ (**5A**) is built from **4A** by terminally coordinating CO to Ce. Similar observation is also obtained for $\text{LaNi}(\text{CO})_n^-$ (Figure S5). Summarizing, a building block of one side-on-bonded CO molecule is favored in the heterobinuclear $\text{LnNi}(\text{CO})_n^-$ ($\text{Ln} = \text{La}, \text{Ce}; n \leq 3$) clusters, whereas a new motif of two side-on-bonded CO molecules is preferred in the $n \geq 4$ clusters.

For the most stable isomers of $\text{CeNi}(\text{CO})_n^-$ ($n = 2-5$) (**2A-5A**), the highest occupied molecular orbitals (HOMO) down to the fourth valence molecular orbital from the HOMO are shown in Figure S6. For **2A**, the α -HOMO is a predominately s-type character, the α -HOMO-1 is π type bond, and the α -HOMO-2, α -HOMO-3, and α -HOMO-4 are featured by the delocalized π orbitals. This implies that the interaction of CO molecules with the CeNi binuclear cluster is stabilized by the π -type bonds. Such bonding mechanism has also been found in isomer **3A**. In isomers **4A** and **5A**, the α -HOMOs feature π -type bonds with striking metal to carbonyl donation, resulting in the significant weakening of C–O bonds.

The terminal and bridging bonding of CO on metal catalyst is a well-known common feature. The extreme weakening of C–O bond has been observed for some transition metal surfaces, where the C–O vibrational stretching frequencies of chemisorbed CO appear in the 1100–1400 cm^{-1} region.^{49–51} In general, the terminal, bridging, and side-on-bonded modes of metal–CO coordination point to the weak, moderate, and extreme C–O bond activation. It can be seen from the above structural analysis of the heterobinuclear $\text{LnNi}(\text{CO})_n^-$ ($\text{Ln} = \text{La}, \text{Ce}$) carbonyls that the number of extremely activated CO molecule is increased in the larger clusters ($n \geq 4$), evidencing the ligand-enhanced CO activation by the early lanthanide–nickel heterodimers. This is different from the structural evolutions of other homobinuclear, heterobinuclear metal–iron, and metal–nickel carbonyls.^{31–39} In the $\text{Ti}_2(\text{CO})_n^-$ ($n = 1-9$) clusters, the building block of three side-on-bonded CO molecules is favored for $n = 3-5$, whereas the motif of two side-on-bonded CO molecules is preferred for $n = 6-9$, indicating that the number of extremely activated CO molecule is reduced in the larger clusters.²⁸ In the $\text{MNi}(\text{CO})_n^-$ ($\text{M} = \text{Ti}, \text{Zr}, \text{Hf}$) complexes, the $n = 3$ cluster is comprised of one terminal, one bridging, and one side-on-bonded carbonyl, whereas the binding motif of three bridging carbonyls is preferred in $n = 4-7$, also suggesting that the degree of CO activation is reduced in the larger clusters.³⁷

Present experimental and theoretical results show the ligand-enhanced CO activation by the early lanthanide–nickel heterodimers. This is reminiscent of the effect of expanded coordination on the CO_2 activation by metals. For instance, infrared photodissociation (IRPD) spectroscopy of $[\text{V}(\text{CO}_2)_n]^+$ clusters revealed that the CO_2 molecule is directly bound to the metal cations in an “end-on” configuration in the $n < 7$ clusters, whereas an oxalate-type C_2O_4 anion species is formed in the $n \geq 7$ clusters.⁵² IRPD spectroscopy of $[\text{Bi}(\text{CO}_2)_n]^-$ clusters demonstrated the motif switch from metalloformate to oxalate with increasing the CO_2 ligands.⁵³ Together with the current findings, these results show how the ligand environment can affect the performance of a catalyst, which would have important implications for uncovering many facets of catalytic

activation/reduction of various important molecules (i.e., CO, CO_2 , N_2 , CH_4 , etc.) at the molecular level and offering design criteria for atom/cluster catalyst engineering.

6. CONCLUSION

The interaction of CO with the lanthanum–nickel and cerium–nickel heterodimers has been studied by photoelectron spectroscopy and quantum chemical calculations. While the binding motif in the most stable isomers of $\text{LnNi}(\text{CO})_n^-$ ($\text{Ln} = \text{La}, \text{Ce}; n = 2$ and 3) consists of one side-on-bonded carbonyl, a new building block of two side-on-bonded carbonyls is favored $n = 4$ and 5. Experimental and theoretical results reveal the ligand-enhanced CO activation by the early lanthanide–nickel heterodimers, which provides detailed insights into the microscopic mechanism of catalytic CO activation.

■ ASSOCIATED CONTENT

Supporting Information

The Supporting Information is available free of charge on the ACS Publications website at DOI: 10.1021/acs.jpca.8b02254.

Time-of-flight mass spectra (Figures S1 and S2) and 355 nm photoelectron images and spectra (Figures S3 and S4) of $\text{LnNi}(\text{CO})_n^-$ ($\text{Ln} = \text{Ce}, \text{La}$), optimized structures of $\text{LaNi}(\text{CO})_n^-$ (Figure S5), molecular orbital pictures of the most stable isomers for $\text{CeNi}(\text{CO})_n^-$ ($n = 2-5$) (Figure S6), and comparison of experimental VDE and ADE values to the TPSSH calculated ones of the isomers for $\text{CeNi}(\text{CO})_n^-$ ($n = 2-5$) (Table S1). (PDF)

■ AUTHOR INFORMATION

Corresponding Author

*(L.J.) E-mail: ljiang@dicp.ac.cn.

ORCID

Ling Jiang: 0000-0002-8485-8893

Author Contributions

[§]These authors contributed equally to this work.

Notes

The authors declare no competing financial interest.

■ ACKNOWLEDGMENTS

This work was supported by the National Natural Science Foundation of China (Grant Nos. 21327901, 21503222, 21673231, and 21688102), the Key Research Program (Grant No. KGZD-EW-T05), and the Strategic Priority Research Program (Grant No. XDB17000000) of the Chinese Academy of Science.

■ REFERENCES

- (1) Castleman, A. W.; Keesee, R. G. Clusters - Bridging the Gas and Condensed Phases. *Acc. Chem. Res.* **1986**, *19*, 413–419.
- (2) Bohme, D. K.; Schwarz, H. Gas-Phase Catalysis by Atomic and Cluster Metal Ions: The Ultimate Single-Site Catalysts. *Angew. Chem., Int. Ed.* **2005**, *44*, 2336–2354.
- (3) Freund, H. J.; Meijer, G.; Scheffler, M.; Schlogl, R.; Wolf, M. CO Oxidation as a Prototypical Reaction for Heterogeneous Processes. *Angew. Chem., Int. Ed.* **2011**, *50*, 10064–10094.
- (4) Lang, S. M.; Bernhardt, T. M. Gas Phase Metal Cluster Model Systems for Heterogeneous Catalysis. *Phys. Chem. Chem. Phys.* **2012**, *14*, 9255–9269.
- (5) Asmis, K. R. Structure Characterization of Metal Oxide Clusters by Vibrational Spectroscopy: Possibilities and Prospects. *Phys. Chem. Chem. Phys.* **2012**, *14*, 9270–9281.

- (6) Ding, X.-L.; Wu, X.-N.; Zhao, Y.-X.; He, S.-G. C-H Bond Activation by Oxygen-Centered Radicals over Atomic Clusters. *Acc. Chem. Res.* **2012**, *45*, 382–390.
- (7) Weber, J. M. The Interaction of Negative Charge with Carbon Dioxide - Insight into Solvation, Speciation and Reductive Activation from Cluster Studies. *Int. Rev. Phys. Chem.* **2014**, *33*, 489–519.
- (8) Luo, Z.; Castleman, A. W., Jr.; Khanna, S. N. Reactivity of Metal Clusters. *Chem. Rev.* **2016**, *116*, 14456–14492.
- (9) Schwarz, H. Metal-Mediated Activation of Carbon Dioxide in the Gas Phase: Mechanistic Insight Derived from a Combined Experimental/Computational Approach. *Coord. Chem. Rev.* **2017**, *334*, 112–123.
- (10) Wang, P.; Xie, H.; Guo, J.; Zhao, Z.; Kong, X.; Gao, W.; Chang, F.; He, T.; Wu, G.; Chen, M.; et al. The Formation of Surface Lithium-Iron Ternary Hydride and its Function on Catalytic Ammonia Synthesis at Low Temperatures. *Angew. Chem., Int. Ed.* **2017**, *56*, 8716–8720.
- (11) Zhou, M.; Andrews, L.; Bauschlicher, C. W., Jr. Spectroscopic and Theoretical Investigations of Vibrational Frequencies in Binary Unsaturated Transition-Metal Carbonyl Cations, Neutrals, and Anions. *Chem. Rev.* **2001**, *101*, 1931–1961.
- (12) Xu, Q. Metal Carbonyl Cations: Generation, Characterization and Catalytic Application. *Coord. Chem. Rev.* **2002**, *231*, 83–108.
- (13) Ricks, A. M.; Reed, Z. E.; Duncan, M. A. Infrared Spectroscopy of Mass-Selected Metal Carbonyl Cations. *J. Mol. Spectrosc.* **2011**, *266*, 63–74.
- (14) Ignatyev, I. S.; Schaefer, H. F.; King, R. B.; Brown, S. T. Binuclear Homoleptic Nickel Carbonyls: Incorporation of Ni–Ni Single, Double, and Triple Bonds, $\text{Ni}_2(\text{CO})_x$ ($x = 5, 6, 7$). *J. Am. Chem. Soc.* **2000**, *122*, 1989–1994.
- (15) Xie, Y. M.; Schaefer, H. F.; King, R. B. Binuclear Homoleptic Iron Carbonyls: Incorporation of Formal Iron–Iron Single, Double, Triple, and Quadruple Bonds, $\text{Fe}_2(\text{CO})_x$ ($x = 9, 8, 7, 6$). *J. Am. Chem. Soc.* **2000**, *122*, 8746–8761.
- (16) Moore, D. T.; Oomens, J.; Eyler, J. R.; Meijer, G.; von Helden, G.; Ridge, D. P. Gas-Phase IR Spectroscopy of Anionic Iron Carbonyl Clusters. *J. Am. Chem. Soc.* **2004**, *126*, 14726–14727.
- (17) Jiang, L.; Xu, Q. Observation of Anomalous C-O Bond Weakening on Discandium and Activation Process to CO Dissociation. *J. Am. Chem. Soc.* **2005**, *127*, 42–43.
- (18) Xu, Q.; Jiang, L.; Tsumori, N. $\text{cyclo-Ti}_3[\eta^2(\mu_2\text{-C}, \text{O})]_3$: A Side-on-Bonded Polycarbonyl Titanium Cluster with Potentially Antiaromatic Character. *Angew. Chem., Int. Ed.* **2005**, *44*, 4338–4342.
- (19) Jin, X.; Jiang, L.; Xu, Q.; Zhou, M. F. Reactions of Gadolinium Atoms and Dimers with CO: Formation of Gadolinium Carbonyls and Photoconversion to CO Activated Molecules. *J. Phys. Chem. A* **2006**, *110*, 12585–12591.
- (20) Xu, Q.; Jiang, L.; Zou, R. Q. Infrared Spectroscopic and Density Functional Theory Investigations of the LaCO , $\text{La}_2[\eta^2(\mu_2\text{-C}, \text{O})]$, and $c\text{-La}_2(\mu\text{-C})(\mu\text{-O})$ Molecules in Solid Argon. *Chem. - Eur. J.* **2006**, *12*, 3226–3232.
- (21) Zhou, M. F.; Jin, X.; Li, J. Reactions of Cerium Atoms and Dicerium Molecules with CO: Formation of Cerium Carbonyls and Photoconversion to CO-Activated Insertion Molecules. *J. Phys. Chem. A* **2006**, *110*, 10206–10211.
- (22) Jiang, L.; Jin, X.; Zhou, M.; Xu, Q. CO Activation on the Late Lanthanide Dimers: Matrix Infrared Spectra of the $\text{Ln}_2(\text{CO})_x$ ($\text{Ln} = \text{Tb}, \text{Dy}, \text{Ho}, \text{Er}, \text{Lu}$; $x = 1, 2$) Molecules. *J. Phys. Chem. A* **2008**, *112*, 3627–3630.
- (23) Jiang, L.; Xu, Q. Theoretical Study of the Interaction of Carbon Monoxide with 3d Metal Dimers. *J. Chem. Phys.* **2008**, *128*, 124317.
- (24) Swart, I.; de Groot, F. M.; Weckhuysen, B. M.; Rayner, D. M.; Meijer, G.; Fielicke, A. The Effect of Charge on CO Binding in Rhodium Carbonyls: From Bridging to Terminal CO. *J. Am. Chem. Soc.* **2008**, *130*, 2126–2127.
- (25) Fielicke, A.; Gruene, P.; Meijer, G.; Rayner, D. M. The Adsorption of CO on Transition Metal Clusters: A Case Study of Cluster Surface Chemistry. *Surf. Sci.* **2009**, *603*, 1427–1433.
- (26) Chi, C. X.; Cui, J. M.; Li, Z. H.; Xing, X. P.; Wang, G. J.; Zhou, M. F. Infrared Photodissociation Spectra of Mass Selected Homoleptic Dinuclear Iron Carbonyl Cluster Anions in the Gas Phase. *Chem. Sci.* **2012**, *3*, 1698–1706.
- (27) Wang, G. J.; Cui, J. M.; Chi, C. X.; Zhou, X. J.; Li, Z. H.; Xing, X. P.; Zhou, M. F. Bonding in Homoleptic Iron Carbonyl Cluster Cations: A Combined Infrared Photodissociation Spectroscopic and Theoretical Study. *Chem. Sci.* **2012**, *3*, 3272–3279.
- (28) Zou, J.; Xie, H.; Dai, D.; Tang, Z.; Jiang, L. Sequential Bonding of CO Molecules to A Titanium Dimer: A Photoelectron Velocity-Map Imaging Spectroscopic and Theoretical Study of $\text{Ti}_2(\text{CO})_n^-$ ($n = 1-9$). *J. Chem. Phys.* **2016**, *145*, 184302.
- (29) Wang, G.; Zhou, M. Infrared Spectra, Structures and Bonding of Binuclear Transition Metal Carbonyl Cluster Ions. *Chin. J. Chem. Phys.* **2018**, *31*, 1–11.
- (30) Schwarz, H. Doping Effects in Cluster-Mediated Bond Activation. *Angew. Chem., Int. Ed.* **2015**, *54*, 10090–10100.
- (31) Liu, Z.; Xie, H.; Qin, Z.; Fan, H.; Tang, Z. Structural Evolution of Homoleptic Heterodinuclear Copper-Nickel Carbonyl Anions Revealed Using Photoelectron Velocity-Map Imaging. *Inorg. Chem.* **2014**, *53*, 10909–10916.
- (32) Zhang, N.; Luo, M.; Chi, C.; Wang, G.; Cui, J.; Zhou, M. Infrared Photodissociation Spectroscopy of Mass-Selected Heteronuclear Iron-Copper Carbonyl Cluster Anions in the Gas Phase. *J. Phys. Chem. A* **2015**, *119*, 4142–4150.
- (33) Xie, H.; Zou, J.; Yuan, Q.; Fan, H.; Tang, Z.; Jiang, L. Photoelectron Velocity-Map Imaging and Theoretical Studies of Heteronuclear Metal Carbonyls $\text{MNi}(\text{CO})_3^-$ ($M = \text{Mg}, \text{Ca}, \text{Al}$). *J. Chem. Phys.* **2016**, *144*, 124303.
- (34) Liu, Z.; Zou, J.; Qin, Z.; Xie, H.; Fan, H.; Tang, Z. Photoelectron Velocity Map Imaging Spectroscopy of Lead Tetracarbonyl-Iron Anion $\text{PbFe}(\text{CO})_4^-$. *J. Phys. Chem. A* **2016**, *120*, 3533–3538.
- (35) Liu, Z.; Xie, H.; Zou, J.; Fan, H.; Tang, Z. Observation of Promoted C-O Bond Weakening on the Heterometallic Nickel-Silver: Photoelectron Velocity-Map Imaging Spectroscopy of $\text{AgNi}(\text{CO})_n^-$. *J. Chem. Phys.* **2017**, *146*, 244316.
- (36) Qu, H.; Kong, F.; Wang, G.; Zhou, M. Infrared Photodissociation Spectroscopy of Heterodinuclear Iron-Zinc and Cobalt-Zinc Carbonyl Cation Complexes. *J. Phys. Chem. A* **2017**, *121*, 1627–1632.
- (37) Zou, J.; Xie, H.; Yuan, Q.; Zhang, J.; Dai, D.; Fan, H.; Tang, Z.; Jiang, L. Probing the Bonding of CO to Heteronuclear Group 4 Metal-Nickel Clusters by Photoelectron Spectroscopy. *Phys. Chem. Chem. Phys.* **2017**, *19*, 9790–9797.
- (38) Chi, C.; Wang, J. Q.; Qu, H.; Li, W. L.; Meng, L.; Luo, M.; Li, J.; Zhou, M. Preparation and Characterization of Uranium-Iron Triple-Bonded $\text{UFe}(\text{CO})_3^-$ and $\text{OUFe}(\text{CO})_3^-$ Complexes. *Angew. Chem., Int. Ed.* **2017**, *56*, 6932–6936.
- (39) Qu, H.; Kong, F.; Wang, G.; Zhou, M. Infrared Photodissociation Spectroscopic and Theoretical Study of Heteronuclear Transition Metal Carbonyl Cluster Cations in the Gas Phase. *J. Phys. Chem. A* **2016**, *120*, 7287–7293.
- (40) Binnemans, K. Lanthanide-Based Luminescent Hybrid Materials. *Chem. Rev.* **2009**, *109*, 4283–4374.
- (41) Wang, F.; Liu, X. Recent Advances in the Chemistry of Lanthanide-Doped Upconversion Nanocrystals. *Chem. Soc. Rev.* **2009**, *38*, 976–989.
- (42) Buenzli, J.-C. G. Lanthanide Luminescence for Biomedical Analyses and Imaging. *Chem. Rev.* **2010**, *110*, 2729–2755.
- (43) Mond, L.; Langer, C.; Quincke, F. Action of Carbon Monoxide on Nickel. *J. Chem. Soc., Trans.* **1890**, *57*, 749–753.
- (44) Qin, Z.; Wu, X.; Tang, Z. Note: A Novel Dual-Channel Time-Of-Flight Mass Spectrometer for Photoelectron Imaging Spectroscopy. *Rev. Sci. Instrum.* **2013**, *84*, 066108.
- (45) Dribinski, V.; Ossadtchi, A.; Mandelshtam, V. A.; Reisler, H. Reconstruction of Abel-Transformable Images: The Gaussian Basis-Set Expansion Abel Transform Method. *Rev. Sci. Instrum.* **2002**, *73*, 2634–2642.

(46) TURBOMOLE V6.4, 2012, a Development of University of Karlsruhe and Forschungszentrum Karlsruhe GmbH, 1989–2007: TURBOMOLE GmbH: 2007.

(47) Frisch, M. J.; Trucks, G. W.; Schlegel, H. B.; Scuseria, G. E.; Robb, M. A.; Cheeseman, J. R.; Scalmani, G.; Barone, V.; Mennucci, B.; Petersson, G. A., et al. *Gaussian 09*; Gaussian, Inc.: Wallingford, CT, 2009.

(48) Wu, H. B.; Wang, L. S. Photoelectron Spectroscopy and Electronic Structure of ScO_n^- ($n = 1-4$) and YO_n^- ($n = 1-5$): Strong Electron Correlation Effects in ScO^- and YO^- . *J. Phys. Chem. A* **1998**, *102*, 9129–9135.

(49) Hoffmann, F. M.; de Paola, R. A. Anomalous C-O Bond Weakening of Side-On-Bonded Carbon Monoxide on a Potassium-Promoted Ru(001) Surface. *Phys. Rev. Lett.* **1984**, *52*, 1697–1700.

(50) Shinn, N. D.; Madey, T. E. Unusual C-O Bond Weakening on a Clean Metal Surface: CO on Cr(110). *Phys. Rev. Lett.* **1984**, *53*, 2481–2484.

(51) Moon, D. W.; Bernasek, S. L.; Dwyer, D. J.; Gland, J. L. Observation of an Unusually Low CO Stretching Frequency on Fe(100). *J. Am. Chem. Soc.* **1985**, *107*, 4363–4364.

(52) Ricks, A. M.; Brathwaite, A. D.; Duncan, M. A. IR Spectroscopy of Gas Phase $\text{V}(\text{CO}_2)_n^+$ Clusters: Solvation-Induced Electron Transfer and Activation of CO_2 . *J. Phys. Chem. A* **2013**, *117*, 11490–11498.

(53) Thompson, M. C.; Ramsay, J.; Weber, J. M. Solvent-Driven Reductive Activation of CO_2 by Bismuth: Switching from Metalloformate Complexes to Oxalate Products. *Angew. Chem., Int. Ed.* **2016**, *55*, 15171–15174.